Inorganic Chemistry

Article

pubs.acs.org/IC

Scan Rate Dependent Spin Crossover Iron(II) Complex with Two Different Relaxations and Thermal Hysteresis *fac*-$[Fe^{II}(HL^{n\text{-}Pr})_3]Cl{\cdot}PF_6$ ($HL^{n\text{-}Pr}$ = 2-Methylimidazol-4-yl-methylideneamino-*n*-propyl)

Takeshi Fujinami,[†] Koshiro Nishi,[†] Daisuke Hamada,[†] Keishiro Murakami,[†] Naohide Matsumoto,*[,†] Seiichiro Iijima,[‡] Masaaki Kojima,[§] and Yukinari Sunatsuki*[,§]

[†]Department of Chemistry, Faculty of Science, Kumamoto University, Kurokami 2-39-1, Kumamoto 860-8555, Japan

[‡]National Institute of Advanced Industrial Science and Technology, Tsukuba 305-8566, Japan

[§]Department of Chemistry, Faculty of Science, Okayama University, Tsushima-naka 3-1-1, Okayama 700-8530, Japan

Supporting Information

ABSTRACT: Solvent-free spin crossover Fe^{II} complex *fac*-$[Fe^{II}(HL^{n\text{-}Pr})_3]Cl{\cdot}PF_6$ was prepared, where $HL^{n\text{-}Pr}$ denotes 2-methylimidazol-4-yl-methylideneamino-*n*-propyl. The magnetic susceptibility measurements at scan rate of 0.5 K min^{-1} showed two successive spin transition processes consisting of the first spin transition T_1 centered at 122 K ($T_{1\uparrow}$ = 127.1 K, $T_{1\downarrow}$ = 115.8 K) and the second spin transition T_2 centered at ca. 105 K ($T_{2\uparrow}$ = 115.8 K, $T_{2\downarrow}$ = 97.2 K). The magnetic susceptibility measurements at the scan rate of 2.0, 1.0, 0.5, 0.25, and 0.1 K min^{-1} showed two scan speed dependent spin transitions, while the Mössbauer spectra detected only the first spin transition T_1. The crystal structures were determined at 160, 143, 120, 110, 95 K in the cooling mode, and 110, 120, and 130 K in the warming mode so as to follow the spin transition process of high-spin HS → HS(T_1) → HS(T_2) → low-spin LS → LS(T_2) → LS(T_1) → HS. The crystal structures at all temperatures have a triclinic space group $P\bar{1}$ with Z = 2. The complex-cation has an octahedral N_6 coordination geometry with three bidentate ligands and assume a *facial*-isomer with Δ- and Λ-enantiomorphs. Three imidazole groups of *fac*-$[Fe^{II}(HL^{n\text{-}Pr})_3]^{2+}$ are hydrogen-bonded to three Cl^- ions. The 3:3 NH(imidazole)···Cl^- hydrogen-bonds form a stepwise ladder assembly structure, which is maintained during the spin transition process. The spin transition process is related to the structural changes of the FeN_6 coordination environment, the order−disorder of PF_6^- anion, and the conformation change of *n*-propyl groups. The Fe−N bond distance in the HS state is longer by 0.2 Å than that in the LS state. Disorder of PF_6^- anion is not observed in the LS state but in the HS state. The conformational changes of *n*-propyl groups are found in the spin transition processes except for HS → HS(T_1) → HS(T_2).

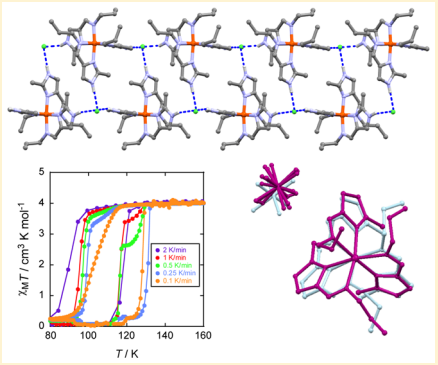

INTRODUCTION

The spin crossover (SCO) phenomenon is a representative example of molecular bistability, in which the high-spin (HS) and low-spin (LS) states of octahedral $3d^n$ ($4 \le n \le 7$) metal complexes are interconvertible by physical perturbations such as temperature and light irradiation.[1] SCO is essentially a phenomenon that originated from a single molecule, as supported by the fact that SCO can be observed in dilute solution. The SCO molecule exhibits the structural changes of molecular size and shape of the SCO center (Fe−N bond lengths and N−Fe−N angles). In the solid state, the structural changes generated by the spin transition propagate from one SCO center to another through elastic interactions mediated by intermolecular contacts. The SCO properties such as gradual-steep and multistep SCO profile, hysteresis, and LIESST (light-induced excited spin state trapping) are governed by the intermolecular contacts between SCO center, i.e, cooperative interaction.[1−3]

In order to achieve the useful SCO parameters of wide thermal hysteresis, spin transition temperature, and multistep SCO, SCO Fe^{II} complexes with $3d^6$ electronic configuration have been intensively studied, and several synthetic designs have been successful.[1] Several representative examples are described. (1) Polynuclear and polymeric SCO complexes can be bridged by rigid ligands.[4] Most of these SCO complexes gave gradual spin transition without thermal hysteresis, demonstrating the negative effect of rigid coordination-bridge.[4] Exceptional compounds are tris-triazole-bridged one-dimensional Fe^{II} complexes $[Fe^{II}(R\text{-}tria)_3]Y_2$ (R = NH_2, 3-hydroxypropyl; Y = BF_4)[2a−c] and *N*-(pyrid-4-yl)-isonicotinamide (pina) bridged 1D Fe^{II} coordination polymer $[Fe^{II}L(pina)]$solvent (L = [3,3′]-[1,2-phenylenebis-(iminomethylidyne)]bis(2,4-pentanedionato)*N*,*N*′,O^2,$O^{2\prime}$).[2d] (2) Mononuclear SCO complexes can exhibit weak inter-

Received: March 27, 2015
Published: July 22, 2015

DOI: 10.1021/acs.inorgchem.5b00701
Inorg. Chem. 2015, 54, 7291−7300

molecular interactions such as hydrogen-bonding[5] and $\pi-\pi$ stacking.[6] Weber and co-workers reported the solvent-free Fe^{II} complex with the widest thermal hysteresis $[Fe^{II}L(Him)]$ (Him = imidazole), whose crystal structure determined at the LS state is constructed by two-dimensional hydrogen-bondings.[3] (3) Hoffman-type SCO complexes give noticeable SCO materials. Because the SCO sites are indirectly connected in the 2D network of the porous 3D framework, the SCO site can be a proper sustainable environment to give useful SCO properties.[7]

It has been well-known that SCO phenomena are highly affected by crystal solvent as well as subtle factors such as order−disorder of the components[8] and ligand conformational change.[8] The large hysteresis often disappears or changes significantly associated with the elimination of the crystal solvent.[2d,6] Although the structural information at all the spin states is essential to elucidate the mechanism of interesting SCO complexes with abrupt or/and multistep SCO and large thermal hysteresis, the crystal structures for SCO complexes could not be determined at all the spin states due to the crash of the crystal during the spin transition. The detailed correlation between structure and SCO property is not fully investigated. We and Brewers have studied the metal complexes of imidazole containing polydentate ligands. The Fe^{II} complexes with imidazole containing polydentate ligands provide a suitable ligand field strength close to the SCO point; form a variety of network structures constructed by hydrogen-bonds, resulting in SCO properties involving steep, multistep SCO, hysteresis, and LIESST; and give suitable compounds to determine the crystal structure at all the spin states.[9,10] The crystal structure consists of a hydrogen-bonded network extended over the crystal lattice, and the structural change associated with SCO transition can be sustainable.

In our previous paper, we reported the syntheses, a variety of network structures constructed by imidazole···chloride hydrogen-bonds including 2D and 3D networks, stepwise ladder, and cubane-like structures, and various SCO properties with one-step and multistep SCO with thermal hysteresis of *fac*-$[Fe^{II}(HL^{n\text{-}R})_3]Cl\cdot Y$ (HL^{R} = 2-methylimidazol-4-yl-methylideneamino-*n*-alkyl; Y = BF_4, PF_6, AsF_6, SbF_6),[11] demonstrating that the SCO properties can be appeared by the slight modification of the component. In this study, we prepared a solvent-free spin crossover Fe^{II} complex **1** with the formula of *fac*-$[Fe^{II}(HL^{n\text{-}Pr})_3]Cl\cdot PF_6$ and focused on the SCO property, as shown in Scheme 1. Complex **1** showed an unusual two successive spin transition processes of the first spin transition T_1 ($T_{1\uparrow}$ = 127.1 K and $T_{1\downarrow}$ = 115.8 K) and the second spin transition T_2 ($T_{2\uparrow}$ = 115.8 K and $T_{2\downarrow}$ = 97.2 K) by the magnetic susceptibility measurement at the scan speed of 0.5 K min^{-1}. The SCO property shows a high scan speed dependence like those in the recent literature.[12] In order to understand the detailed mechanism of the unusual SCO profile, the scan speed and particle size dependence of the magnetic susceptibilities, Mössbauer spectra, and the single-crystal X-ray structures were carried out. Owing to the network structure constructed by the imidazole···chloride hydrogen-bond, the crystal structures were determined so as to follow the spin transition process of high-spin HS → HS(T_1) → HS(T_2) → low-spin LS → LS(T_2) → LS(T_1) → HS, and the detailed structural information to examine the SCO mechanism was obtained. The HS and LS structures at 120 K (T_1 region) in the cooling and heating modes were determined. The structures at 110 K (T_2 region) in the cooling and heating modes are also determined. We report here the results of the magnetic susceptibilities, the Mössbauer spectra, and the X-ray diffraction analyses of scan rate dependent SCO Fe^{II} complex with slow and fast relaxations and thermal hysteresis.

Scheme 1. Δ-*fac*-$[Fe^{II}(HL^{n\text{-}Pr})_3]^{2+}$

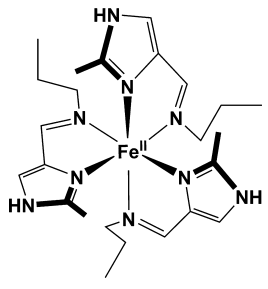

EXPERIMENTAL SECTION

Materials. All reagents and solvents used in this study are commercially available from Tokyo Kasei Co., Ltd., Tokyo and Wako Pure Chemical Industries, Ltd. Tokyo. They were used without further purification. All the synthetic procedures were performed in an open atmosphere.

***fac*-$[Fe^{II}(HL^{n\text{-}Pr})_3]Cl\cdot PF_6$ (1).** To a solution of *n*-propylamine (0.177 g, 3 mmol) in 5 mL of methanol was added a solution of 2-methyl-4-formylimidazole (0.330 g, 3 mmol) in 5 mL of methanol at room temperature. The resulting solution was warmed at 50 °C under stirring for 30 min and then cooled to room temperature, giving the ligand solution of 2-methylimidazol-4-yl-methylideneamino-*n*-propyl (abbreviated as $HL^{n\text{-}Pr}$). To the ligand solution thus prepared (3 mmol) was added a solution of $Fe^{II}Cl_2\cdot 4H_2O$ (0.199 g, 1 mmol) in 10 mL of methanol at room temperature. To the mixture was added a solution of $NaPF_6$ (0.168 g, 1 mmol) in 5 mL of methanol. The resulting solution was stirred at room temperature for 1 h and then filtered. The filtrate was kept for a few days for slow evaporation in air, during which time yellow block crystals precipitated. They were collected by suction filtration, and washed with small amount of water. Yield: 0.22 g. Anal. Calcd for $[Fe(HL^{n\text{-}Pr})_3]Cl\cdot PF_6$ = $C_{24}H_{39}FeN_9ClPF_6$: C, 41.78; H, 5.70; N, 18.27. Found: C, 41.85; H, 5.67; N, 18.05. FAB-MS. Calcd for $[(HL^{n\text{-}Pr}) + H^+]^+$: *m*/*z* 152.2. Found: *m*/*z* 152.2. Calcd for $\{[Fe^{II}(HL^{n\text{-}Pr})]^{2+} - H^+\}^+$: *m*/*z* 206.0. Found: *m*/*z* 206.1. Calcd for $\{[Fe^{II}(HL^{n\text{-}Pr})_2]^{2+} - H^+\}^+$: *m*/*z* 357.3. Found: *m*/*z* 357.3. Calcd for $\{[Fe^{II}(HL^{n\text{-}Pr})_3]^{2+} - H^+\}^+$: *m*/*z* 508.5. Found: *m*/*z* 508.4. Calcd for $\{[Fe^{II}(HL^{n\text{-}Pr})_3]^{2+} + PF_6^-\}^+$: *m*/*z* 654.4. Found: *m*/*z* 654.5. TG/DTA: weight loss less than 0.2% was observed in the heating process from room temperature to 120 °C.

Physical Measurements. Elemental C, H, and N analyses and FAB-MS spectra were carried out at the Center for Instrumental Analysis of Kumamoto University. Thermogravimetric analyses (TGAs) were performed on a TG/DTA6200 (Seiko Instrument Inc.). The sample of ca. 2 mg was heated from room temperature to 120 °C in the heating mode at 2 °C min^{-1}, kept at 120 °C for 60 min, and then cooled from 120 °C to room temperature. FAB-MS spectra were measured in methanol on a JEOL JMS-700 mass spectrometer, and 3-nitrobenzylalcohol was used as the matrix. X-ray powder diffraction pattern was measured at room temperature on a Rigaku Rint 2500 powder X-ray diffractometer using graphite monochromated Cu Kα radiation (λ = 0.154 18 nm). Magnetic susceptibilities were measured by a Quantum Design MPMS XL5 magnetometer in the temperature range 5−300 K at the sweep rates 0.1, 0.25, 0.5, 1.0, and 2.0 K min^{-1} under an applied magnetic field of 0.5 T. The calibration was done with palladium metal. Corrections for diamagnetism were made using Pascal's constants.[13] Mössbauer spectra were recorded using a Wissel 1200 spectrometer and a proportional counter. The radioactive source was provided by ^{57}Co(Rh), moving in a constant acceleration mode. Hyperfine parameters were obtained by a least-squares fitting of the Lorentzian peaks by the use of Mössbauer spectrum analysis and database software.[14] Isomer shifts were reported

DOI: 10.1021/acs.inorgchem.5b00701
Inorg. Chem. 2015, 54, 7291−7300

relative to iron foil at 293 K. The sample temperature was controlled by means of a Heli-tran liquid transfer refrigerator (Air Products and Chemicals, Inc.) to an accuracy of ±1 K. After the sample is settled at the temperature for over 6 h, the measurement was started, and it took several days to collect the signals.

Crystallographic Structure Analyses. The single-crystal X-ray diffraction data were collected by a Rigaku RAXIS RAPID imaging plate diffractometer using graphite monochromated Mo Kα radiation (λ = 0.710 73 Å). The temperature of the crystal was maintained at the selected value by means of a Rigaku cooling device within an accuracy of ±2 K. As the magnetic susceptibility and Mössbauer spectra demonstrated that **1** showed SCO property with thermal hysteresis and relaxation process, the X-ray diffraction data were collected at 160, 143, 120, 110, 95 K in the cooling mode, and 110, 120, and 130 K in the warming mode so as to follow the SCO process of high-spin (HS) → low-spin (LS) → high-spin (HS). The crystal was cooled from one to another temperature at a rate of 1 K min^{-1}, and the X-ray diffraction analysis started after the crystal was kept at the temperature for 3 h. In the warming mode, the crystal was warmed at a rate of 0.1 K min^{-1} and kept at the temperature for 3 h, and then X-ray analysis was started. The structures were solved by direct methods and expanded using the Fourier technique. For the structure analysis of (**d**) at 110 K in the cooling mode, the reflection data gives a small ratio of reflections to parameters and isotropic thermal parameters except for Fe, Cl, P, F, and coordinated nitrogen atoms are applied. For the crystal structures of (e) at 95 K, (**f**) at 110 K, and (**g**) at 120 K in the warming mode, the large residual electron densities (highest peak = 3.4, 4.2, and 2.7 e Å^{-3} near to Fe for (**e**), (**f**), and (**g**), respectively) were found in the positions near Fe (ca. 0.03 Å). The smaller electron densities were found near the Cl and P positions. There are no remarkable residual electron densities assignable to the carbon and nitrogen atoms of $[Fe(H_3L^{n\text{-}Pr})_3]^{2+}$ cation and F atoms of PF_6^- anion. Hydrogen atoms were fixed at the calculated positions and refined using a riding model. All calculations were performed using the Crystal Structure crystallographic software package.[15]

RESULTS AND DISCUSSION

Syntheses and Characterization of *fac*-$[Fe^{II}(HL^{n\text{-}Pr})_3]Cl\cdot PF_6$ (1). Bidentate chelate ligand 2-methylimidazol-4-yl-methylideneamino-*n*-propyl, abbreviated as $HL^{n\text{-}Pr}$, was prepared by the 1:1 condensation reaction of 2-methyl-4-formylimidazole and *n*-propylamine in methanol. The ligand solution was used for the synthesis of the Fe^{II} complex without the isolation of the ligand. The mixed solution of the ligand solution, $Fe^{II}Cl_2\cdot 4H_2O$, and $NaPF_6$ in methanol with the 3:1:1 molar ratio was kept to stand for several days in air at ambient temperature. Yellow block crystals with the dimensions of 5 mm or larger sizes of **1** were obtained in methanol. The chemical formula of $[Fe^{II}(HL^{n\text{-}Pr})_3]Cl\cdot PF_6$ was confirmed by the C, H, and N elemental analyses. Thermogravimetric analyses (TGA) showed no existence of crystal solvents as confirmed by observations of weight losses less than 0.2% from room temperature to 120 °C. FAB-MS spectra demonstrated the molecular ion peaks from $[Fe^{II}(HL^{n\text{-}Pr})_3]Cl\cdot PF_6$. Complex **1** showed thermochromism between yellow at room temperature and red at liquid nitrogen temperature in the solid state, which is a typical thermochromism of Fe^{II} SCO complexes with the analogous ligands.

Magnetic Properties of *fac*-$[Fe^{II}(HL^{n\text{-}Pr})_3]Cl\cdot PF_6$ (1). The magnetic susceptibilities of a ground sample were measured upon cooling from 300 to 5 K and then upon warming from 5 to 300 K under 0.5 T applied magnetic field. The measurements were performed at the five scan speeds of 2.0, 1.0, 0.5, 0.25, and 0.1 K min^{-1} with five consecutive cycle runs. The $\chi_M T$ versus T plots for these cycles are shown in Figure 1a. Complex **1** showed scan rate dependent SCO profile consisting of two

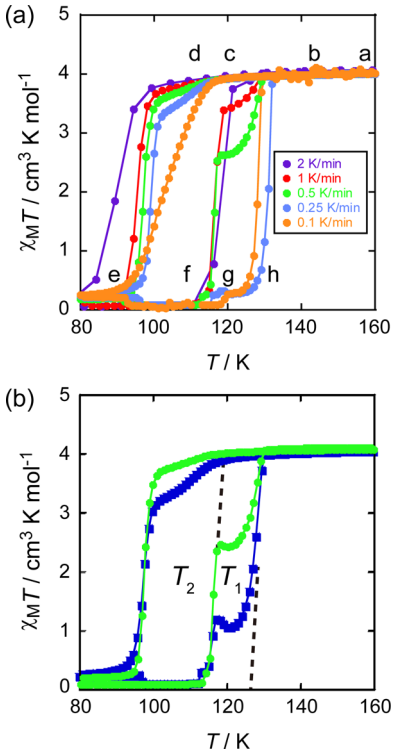

Figure 1. (a) Magnetic behaviors of ground sample of *fac*-$[Fe^{II}(HL^{n\text{-}Pr})_3]Cl\cdot PF_6$ (**1**) in the form of $\chi_M T$ versus T plots at the five scan speeds of 2.0, 1.0, 0.5, 0.25, and 0.1 K min^{-1} with five consecutive cycle runs. (b) Magnetic behaviors of ground sample (green) and well-ground sample (blue) of **1** in the form of $\chi_M T$ versus T plots at 0.5 K min^{-1} scan speed.

spin transition processes with thermal hysteresis. The SCO profile at the scan speed of 0.5 K min^{-1} is represented. In the cooling mode from 300 to 5 K, the $\chi_M T$ value assumes a constant value of ca. 4.0 cm^3 K mol^{-1} in the region 300−120 K, gradually decreases to 3.8 cm^3 K mol^{-1} above ca. 100 K, and decreases abruptly around 97 K to reach 0.2 cm^3 K mol^{-1} below 90 K. The constant $\chi_M T$ value of ca. 4.0 cm^3 K mol^{-1} is larger than the spin-only value of 3.0 cm^3 K mol^{-1} for HS Fe^{II} (S = 2), and is compatible with the reported HS Fe^{II} (S = 2) complexes with the analogous ligands.[8,10] The constant value of 0.2 cm^3 K mol^{-1} below 90 K corresponds to the LS (S = 0) state of the LS Fe^{II} complex. The abrupt spin transition from HS (S = 2) to LS (S = 0) states at the scan speed of 0.5 K min^{-1} occurs at the spin transition temperature $T_{c\downarrow}$ = 97.2 K. On elevating the temperature from 5 to 300 K, the $\chi_M T$ value assumes a constant value at 0.2 cm^3 K mol^{-1} assigned to the LS Fe^{II} species up to ca. 110 K, then increases steeply with two spin transition processes in the region between 110 and 130 K, and finally reaches to the plateau value of 4.0 cm^3 K mol^{-1} assignable to the HS Fe^{II} species at the temperature higher than 130 K. The $\chi_M T$ versus T plots at 0.5 K min^{-1} showed that the two spin transitions T_1 and T_2 occur centered at ca. 125 and ca. 105 K, respectively. The SCO transition temperatures at 0.5 K min^{-1} are T_1 ($T_{1\uparrow}$ = 127.1 K, $T_{1\downarrow}$ = 115.8 K) with 11.3 K wide hysteresis and the spin transition T_2 ($T_{2\uparrow}$ = 115.8 K, $T_{2\downarrow}$ = 97.2 K) with 18.6 K wide hysteresis, in which the two different spin transitions occur subsequently. When the scan speed is varied in the range 0.1−2.0 K min^{-1}, the spin transition temperature of $T_{2\uparrow}$ = 115.8 K in the heating mode is practically invariant, whereas $T_{2\downarrow}$ in the cooling mode is affected by the scan speed,

DOI: 10.1021/acs.inorgchem.5b00701
Inorg. Chem. 2015, 54, 7291−7300

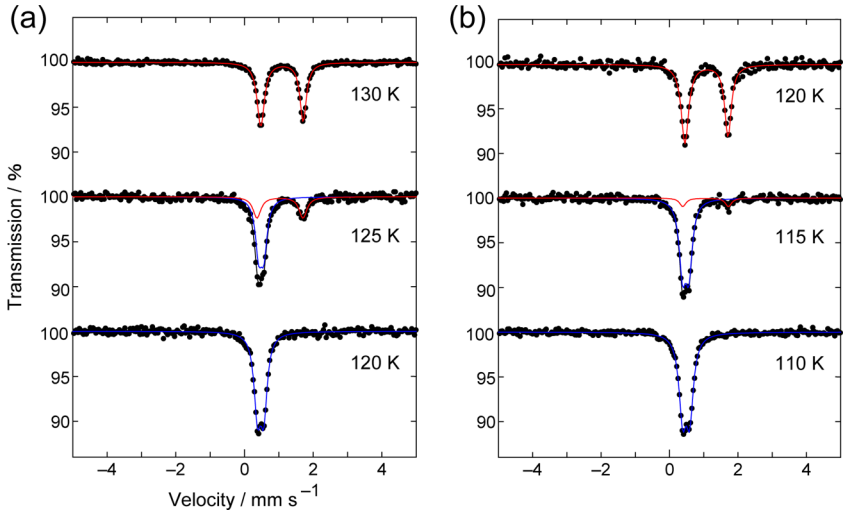

Figure 2. (a) Selected Mössbauer spectra of *fac*-$[Fe(HL^{n\text{-}Pr})_3]Cl{\cdot}PF_6$ (**1**) recorded at 120, 125, and 130 K upon warming the sample after rapid cooling to 78 K. (b) Selected Mössbauer spectra of **1** recorded at 120, 115, and 110 K upon gradual cooling from 298 K.

as confirmed by the data of $T_{2\downarrow}$ = 90.0, 95.0, 97.2, 100.0, and 102.0 K for 2.0, 1.0, 0.5, 0.25, and 0.1 K min^{-1}, respectively. As shown by the above data and Figure 1a, as the scan speed decreases, $T_{2\downarrow}$ increases the temperature, and the hysteresis width of T_2 phase increases. The magnetic profile of fast scan speed experiment suggests the occurrence of a temperature lag due to the freeze-in of the HS state during the HS to LS conversion. As the scan speed is closer to zero, the spin transition of T_2 is disappearing, and in turn the spin transition of T_1 is pronounced. On the other hand, the spin transition T_1 shows a different character from T_2, in which the scan speed does not affect the SCO temperature of $T_{1\uparrow}$ and $T_{1\downarrow}$, but the SCO profile of T_1. As the scan speed decreases, T_1 is appearing, especially as the curve at the higher temperature side at 127 K is pronounced. At the scan speed of 0.1 K min^{-1}, almost complete spin transition T_1 from LS to HS is observed in the warming mode. The similar spin transition properties with multistable SCO phases with two thermal memory channels are found in a mononuclear Fe^{II} complex $[Fe^{II}(n\text{Bu-im})_3(tren)](PF_6)_2$ ((*n*Bu-im)$_3$(tren) is a tripodal N_6 ligand derived from the 3:1 condensation of the *n*-buthylated 1*H*-imidazol-2-aldehyde (*n*Bu-im) and tris(2-ethylamino)amine (tren)), where the order/disorder of PF_6 anion and the conformational change of butyl groups, and the dramatic changes in the crystal packing, are related to the SCO properties.[12b]

To confirm the reproducibility of the hysteretic profile at a scan rate, two cycles of the $\chi_M T$ versus T plots are measured at 0.5 K min^{-1}, and the result is given in Figure S1 of Supporting Information. The profile shows the reproducibility. After the magnetic susceptibility measurement of a ground sample at 0.5 K min^{-1} scan rate, the sample was well-ground, and then the magnetic susceptibilities were measured at 0.5 K min^{-1} scan rate, in order to see the particle size effect on the spin transition profile. The result is shown as $\chi_M T$ versus T plots in Figure 1b. The effect of the sample treatment (particle size) is clearly seen in both the spin transitions of T_1 and T_2. The well-ground sample is very sensitive to their spin transitions for both the spin transitions of T_1 and T_2. The profile of $\chi_M T$ versus T plots demonstrates that the good grinding of the sample (smaller particle size) has the same effect regarding the slower scan speed. The result indicates that the spin transitions of T_1 and T_2 are the relaxation processes.

Mössbauer Spectra of *fac*-$[Fe^{II}(HL^{n\text{-}Pr})_3]Cl{\cdot}PF_6$ (1). The Mössbauer spectra of **1** were measured by the use of the same polycrystalline sample used for the magnetic susceptibility measurement. After rapid cooling from room temperature to 78 K, Mössbauer spectra were recorded in warming mode and then recorded in the cooling mode. Representative Mössbauer spectra in the warming and cooling modes are shown in Figure 2a,b, respectively. A deconvolution analysis of the spectra was performed to determine the HS versus total Fe^{II} molar fraction. The assigned HS and LS spectra at each temperature are shown in Figure 2 as red and blue curves, respectively. The results of the HS versus total Fe^{II} molar fraction are presented in Table 1.

Table 1. Mössbauer Data of *fac*-$[Fe(HL^{n\text{-}Pr})_3]Cl{\cdot}PF_6$ (1)

on heating after rapid cooling down to 78 K					
T/K	δ^a/mm·s^{-1}	ΔE_Q/mm s^{-1}	Γ^b/mm s^{-1}	area ratio/%	assignment
135	1.08	1.22	0.24	100	HS Fe^{II}
130	1.09	1.24	0.24	100	HS Fe^{II}
125	1.04	1.33	0.28	34	HS Fe^{II}
	0.49	0.15	0.23	66	LS Fe^{II}
120	0.47	0.18	0.23	100	LS Fe^{II}
78	0.50	0.29	0.25	100	LS Fe^{II}
on slow cooling from room temperature					
T/K	δ^a/mm s^{-1}	ΔE_Q/mm s^{-1}	Γ^b/mm s^{-1}	area ratio/%	assignment
125	1.08	1.24	0.24	100	HS Fe^{II}
120	1.08	1.26	0.25	100	HS Fe^{II}
115	1.06	1.34	0.22	11	HS Fe^{II}
	0.47	0.18	0.23	89	LS Fe^{II}
110	0.49	0.21	0.26	100	LS Fe^{II}

^{a}Isomer shift data are reported to iron foil. ^{b}Full width at half-height.

Figure 3 shows the HS Fe^{II} molar fraction versus T plots obtained from the Mössbauer measurements as well as those from the magnetic measurements at the scan rate of 0.5 K min^{-1}.

After rapid cooling from room temperature to 78 K, Mössbauer spectra were recorded at 78, 120, 125, 130, and 135 K in the warming mode. The spectrum at 78 and 120 K consists of a doublet attributable to LS Fe^{II} species (δ = 0.50 mm s^{-1}, ΔE_Q = 0.29 mm s^{-1} at 78 K), and the spectrum at 130

DOI: 10.1021/acs.inorgchem.5b00701
Inorg. Chem. 2015, 54, 7291−7300

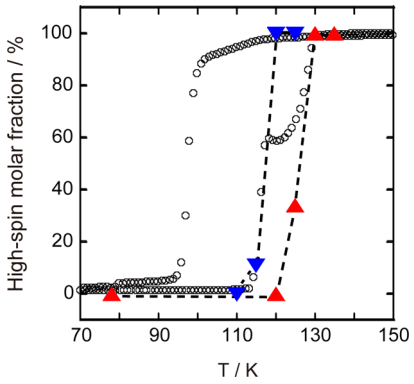

Figure 3. Molar fraction of HS of total Fe^{II} versus T plots for *fac*-$[Fe(HL^{n\text{-}Pr})_3]Cl{\cdot}PF_6$ (**1**) in the warming (red) and cooling (blue) modes obtained by deconvolution analysis of the Mössbauer spectra, together with the molar fraction (○) versus T plots from the magnetic susceptibility measurements at the scan rate of 0.5 K min^{-1}. The HS fraction n_{HS} was calculated by using the equation $(\chi_M T)_{obs} = n_{HS}(\chi_M T)_{HS} + (1 - n_{HS})(\chi_M T)_{LS}$, where $(\chi_M T)_{HS}$ = 4.0 cm^3 K mol^{-1} and $(\chi_M T)_{LS}$ = 0.2 cm^3 K mol^{-1} are used as limiting values.

and 135 K consists of a doublet attributable to the HS Fe^{II} (δ = 1.08 mm s^{-1}, ΔE_Q = 1.22 mm s^{-1} at 135 K). The spectrum at 78 K exhibited no signals attributable to the HS Fe^{II} species, showing no frozen-in effect. At 125 K, the spectrum consists of two doublets attributable to LS and HS Fe^{II} species, showing that the spin transition occurs around the temperature.

In the cooling mode from room temperature, Mössbauer spectra were recorded at 125, 120, 115, and 110 K. The spectrum at 125 K in the cooling mode consists of a doublet attributable to the HS Fe^{II} species, while the spectrum at the same temperature 125 K in the warming mode consists of two doublets attributable to HS and LS Fe^{II} species with the relative area ratio of HS:LS = 34:66. The spectrum at 120 K in the cooling mode consists of a doublet attributable to the HS Fe^{II} species, while the spectrum at the same temperature 120 K in the warming mode consists of a doublet attributable to LS Fe^{II} species. These data are indicative of thermal hysteresis. At 115 and 110 K, the spectrum attributable to LS Fe^{II} species becomes predominant. As shown in Figure 3, the Mössbauer spectral data indicate the one-step steep spin transition around 120 K and thermal hysteresis of ca. 10 K.

The spin transition properties of **1** resulted from the Mössbauer spectral measurements are inconsistent with those of the magnetic susceptibility measurements. The Mössbauer spectra indicate a one-step steep spin transition around 120 K with ca. 10 K wide thermal hysteresis, while the magnetic susceptibilities at 0.5 K min^{-1} demonstrated two types of spin transitions of T_1 around 120 K and T_2 around 105 K. The Mössbauer spectra detected the first spin transition T_1 around 120 K, but not the second spin transition T_2 around 105 K. This is rationalized by the difference of time measurement between magnetic susceptibility and Mössbauer spectra measurements. The Mössbauer measurements were carried out after the sample was settled at the temperature for over 6 h, and the measurement started. It took several days to collect the data at the temperature. The magnetic susceptibilities at the scan speed of 0.5 K min^{-1} take 100 min to sweep a 50 K temperature region and do not reflect well the measurement condition of the Mössbauer spectra. That at the slower scan speed of 0.1 K min^{-1} rather reflects the Mössbauer spectral condition. During the time of Mössbauer measurement, the relaxation from the HS to LS state completes at 110 and 115 K, and the LS state of T_1 is stabilized. It implies that **1** consists of two types of spin transitions which exhibit two different relaxation processes.

Crystal Structure of *fac*-$[Fe^{II}(HL^{n\text{-}Pr})_3]Cl{\cdot}PF_6$ (1). The crystallographic data at 160 (**a**), 143 (**b**), 120 (**c**), 110 (**d**), and 95 (**e**) K in the cooling mode and at 110 (**f**), 120 (**g**), and 130 (**h**) K in the warming mode are listed in Table 2. Relevant bond distances, angles, and hydrogen-bond distances are given in Table 3, where the same atom numbering scheme is taken for all the structures.

Complex **1** crystallizes in a triclinic space group $P\bar{1}$ (No. 2) at all temperatures, while the cell dimensions at all the temperatures are essentially similar but show the significant differences. No crystallographic phase transition is observed during the spin transition. The unique unit consists of one complex-cation $[Fe^{II}(HL^{n\text{-}Pr})_3]^{2+}$, one chloride ion, and one

Table 2. X-ray Crystallographic Data for *fac*-$[Fe^{II}(HL^{n\text{-}Pr})_3]Cl{\cdot}PF_6$ (1) at 160 (a), 143 (b), 120 (c), 110 (d), and 95 (e) K in the Cooling Mode and at 110 (f), 120 (g), and 130 (h) K in the Warming Mode

	fac-$[Fe^{II}(HL^{n\text{-}Pr})_3]Cl{\cdot}PF_6$ (1)[a]							
	cooling mode					warming mode		
	160 K (**a**)	143 K (**b**)	120 K (**c**)	110 K (**d**)	95 K (**e**)	110 K (**f**)	120 K (**g**)	130 K (**h**)
cryst syst	triclinic	triclinic	triclinic	triclinic	triclinic	triclinic	triclinic	triclinic
space group	$P\bar{1}$ (No. 2)	$P\bar{1}$ (No. 2)	$P\bar{1}$ (No. 2)	$P\bar{1}$ (No. 2)	$P\bar{1}$ (No. 2)	$P\bar{1}$ (No. 2)	$P\bar{1}$ (No. 2)	$P\bar{1}$ (No. 2)
a, Å	10.4489(6)	10.4327(7)	10.4153(7)	10.504(10)	10.370(2)	10.386(3)	10.417(2)	10.426(1)
b, Å	12.8038(9)	12.800(1)	12.7968(7)	12.701(9)	12.807(2)	12.829(3)	12.624(2)	12.810(1)
c, Å	12.9986(8)	12.980(1)	12.9483(8)	12.861(10)	12.878(2)	12.883(4)	12.750(2)	12.967(2)
α, deg	85.319(2)	85.205(3)	85.034(2)	85.29(3)	84.742(4)	84.778(6)	85.370(3)	85.164(2)
β, deg	71.832(2)	71.737(2)	71.665(2)	69.45(6)	68.997(3)	69.097(6)	69.861(4)	71.729(3)
γ, deg	80.409(2)	80.440(3)	80.407(2)	83.72(7)	76.904(3)	77.102(7)	83.818(4)	80.404(3)
V, Å^3	1628.4(2)	1622.3(2)	1614.2(2)	1595(3)	1555.0(4)	1563.1(7)	1563.3(5)	1620.6(2)
Z	2	2	2	2	2	2	2	2
D_{calcd}, g cm^{-3}	1.406	1.412	1.419	1.436	1.473	1.466	1.465	1.414
μ, cm^{-1}	6.582	6.606	6.640	6.719	6.892	6.857	6.856	6.613
R[b]	0.0461	0.0464	0.0406	0.0739	0.1013	0.1389	0.1012	0.0773
R_w[c]	0.1411	0.1398	0.1083	0.2062	0.2909	0.3140	0.2324	0.1748

[a]Formula, $C_{24}H_{39}N_9FeClPF_6$; fw 689.90. [b]$R = \sum||F_o| - |F_c||/\sum|F_o|$. [c]$R_w = [\sum w(|F_o^2| - |F_c^2|)^2/\sum w|F_o^2|^2]^{1/2}$.

DOI: 10.1021/acs.inorgchem.5b00701
Inorg. Chem. 2015, 54, 7291−7300

Table 3. Coordination Bond Distances (Å), Hydrogen-Bond Distances (Å), and Bond Angles (deg) for *fac*-$[Fe^{II}(HL^{n\text{-}Pr})_3]Cl\cdot PF_6$ (1) at 160 (a), 143 (b), 120 (c), 110 (d), and 95 (e) K in the Cooling Mode and at 110 (f), 120 (g), and 130 (h) K in the Warming Mode

	fac-$[Fe^{II}(HL^{n\text{-}Pr})_3]Cl\cdot PF_6$ (1)							
	cooling mode					warming mode		
	160 K (a)	143 K (b)	120 K (c)	110 K (d)	95 K (e)	110 K (f)	120 K (g)	130 K (h)
	Coordination Bond Lengths (Å)							
Fe−N(2)	2.178(2)	2.176(3)	2.170(3)	2.024(11)	1.995(6)	1.996(10)	1.991(6)	2.168(5)
Fe−N(3)	2.239(3)	2.237(3)	2.234(3)	2.002(12)	1.980(5)	1.979(9)	1.982(6)	2.237(5)
Fe−N(5)	2.177(2)	2.179(2)	2.171(3)	1.997(12)	1.972(5)	1.983(9)	1.999(6)	2.177(5)
Fe−N(6)	2.190(3)	2.189(3)	2.193(3)	2.013(12)	1.964(6)	1.990(11)	1.993(7)	2.186(5)
Fe−N(8)	2.143(3)	2.142(3)	2.141(3)	2.002(12)	1.967(6)	1.970(12)	1.982(7)	2.141(5)
Fe−N(9)	2.252(3)	2.248(3)	2.246(3)	2.014(12)	2.013(6)	2.023(10)	1.972(6)	2.241(5)
av ⟨Fe−N⟩	2.197(3)	2.195(3)	2.193(3)	2.008(12)	1.982(6)	1.990(10)	1.987(6)	2.192(5)
	Hydrogen-Bond Lengths (Å)							
Cl···N(1)	3.127(3)	3.128(3)	3.132(3)	3.201(13)	3.132(1)	3.132(10)	3.128(7)	3.136(5)
Cl···N(4)	3.121(3)	3.122(3)	3.118(3)	3.146(16)	3.127(6)	3.146(12)	3.095(7)	3.125(6)
Cl···N(7)	3.127(3)	3.123(3)	3.130(3)	3.168(14)	3.091(7)	3.129(12)	3.123(7)	3.130(6)
	Coordination Bond Angles (deg)							
N(2)−Fe−N(3)	76.98(8)	76.96(8)	77.26(9)	79.9(5)	80.5(2)	82.0(4)	81.7(3)	77.1(2)
N(2)−Fe−N(5)	96.54(8)	96.45(8)	96.08(10)	95.3(5)	93.9(2)	92.9(4)	94.9(3)	96.4(2)
N(2)−Fe−N(6)	90.18(9)	90.17(9)	89.98(11)	89.5(5)	90.7(3)	89.3(5)	89.0(3)	90.3(2)
N(2)−Fe−N(8)	98.49(9)	98.51(9)	98.59(11)	96.0(5)	95.1(3)	96.4(5)	95.9(3)	98.6(2)
N(3)−Fe−N(6)	95.23(9)	95.12(9)	95.04(11)	93.2(5)	93.6(3)	94.6(5)	93.7(3)	95.0(2)
N(3)−Fe−N(8)	93.15(9)	93.24(9)	93.24(10)	92.5(5)	91.9(3)	90.2(5)	92.3(3)	93.2(2)
N(3)−Fe−N(9)	103.35(8)	103.45(8)	103.38(9)	97.8(5)	100.8(2)	99.1(4)	96.8(3)	103.5(2)
N(5)−Fe−N(6)	77.69(9)	77.76(9)	77.97(11)	81.5(5)	82.7(3)	81.5(5)	81.7(3)	78.4(2)
N(5)−Fe−N(8)	94.69(9)	94.66(9)	94.53(11)	93.2(5)	92.3(3)	94.1(5)	92.6(3)	94.2(2)
N(5)−Fe−N(9)	83.65(8)	83.68(8)	83.81(10)	87.2(5)	84.9(2)	86.1(4)	86.8(3)	83.6(2)
N(6)−Fe−N(9)	94.21(8)	94.30(8)	94.48(10)	93.0(5)	91.8(3)	92.8(4)	93.8(3)	94.4(2)
N(8)−Fe−N(9)	77.06(9)	76.95(9)	76.85(11)	81.8(5)	82.2(3)	81.4(5)	81.4(3)	76.7(2)

PF_6^- ion. As the representative example, the crystal structure at 95 K is described. The structure of the complex-cation $[Fe^{II}(HL^{n\text{-}Pr})_3]^{2+}$ with the selected atom numbering scheme, together with three hydrogen-bonded Cl^- ions, is shown in Figure 4. The complex-cation has an octahedral N_6 geometry coordinated by three bidentate ligands. The Fe−N(imidazole) distances are shorter than those of Fe−N(imine). The cation has *facial* geometry *fac*-$[Fe^{II}(HL^{n\text{-}Pr})_3]^{2+}$ of two possible *facial* and *meridional* geometrical isomers. The cation is a chiral species with two possible chiral isomers of Δ-*fac*-$[Fe^{II}(HL^{n\text{-}Pr})_3]^{2+}$ and Λ-*fac*-$[Fe^{II}(HL^{n\text{-}Pr})_3]^{2+}$ enantiomorphs due to the clockwise and anticlockwise arrangements of three bidentate ligands around the Fe^{II} ion. Due to the crystallization into a centrosymmetric space group, two enantiomorphs are involved in the crystal.

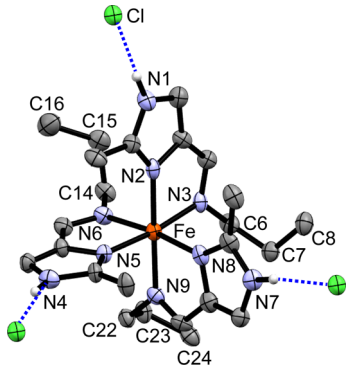

Figure 4. ORTEP drawing of *fac*-$[Fe^{II}(HL^{n\text{-}Pr})_3]^{2+}$ (1) at 95 K viewed along the pseudo-C_3 axis with the selected atom numbering scheme and three hydrogen-bonding manners from a *fac*-$[Fe^{II}(HL^{n\text{-}Pr})_3]^{2+}$ to three neighboring Cl^- ions. Hydrogen atoms except for imidazole hydrogens are omitted for clarity. The thermal ellipsoids were drawn at the 50% probability level.

All three imidazole groups of the *fac*-$[Fe^{II}(HL^{n\text{-}Pr})_3]^{2+}$ are hydrogen-bonded to three Cl^- ions, or from the viewpoint of the Cl^- ion, one Cl^- ion is hydrogen-bonded to three imidazole groups of three neighboring *fac*-$[Fe^{II}(HL^{n\text{-}Pr})_3]^{2+}$ cations (see Figures 4 and 5 and Table 3). The three hydrogen-bond distances are $Cl^-\cdots N(1)$ = 3.132(1) Å, $Cl^-\cdots N(4)$ = 3.127(6) Å, and $Cl^-\cdots N(7)$ = 3.091(7) Å at 95 K. There is no noteworthy difference in three $Cl^-\cdots NH$ hydrogen-bond distances at all the temperatures.

Figure 5a shows a one-dimensional (1D) ladder structure of **1** running along the *a*-axis and the packing manner of the adjacent ladders on *ac*-plane. In the 1D ladder structure, two adjacent cations are bridged by two Cl^- ions. Figure 5b shows the side view of the stepwise ladder structure and accommodation of PF_6^- anions within a ladder, and the stacking manner of the adjacent ladders. The stepwise structure provides void-spaces for accommodation of PF_6^- anions. The accommodated PF_6^- anions have disorder in the HS state at 160, 143, and 120 K in the cooling mode and at 130 K in the warming mode, but the PF_6^- anions have no disorder in the LS state at 95 K in the cooling mode at 110 and 120 K in the warming mode. Figure 5c shows the Δ- and Λ-enantiomorphs of 1D ladder structure and the packing manner of the adjacent ladders, in which the Δ- and Λ-enantiomorphs are represented

DOI: 10.1021/acs.inorgchem.5b00701
Inorg. Chem. 2015, 54, 7291−7300

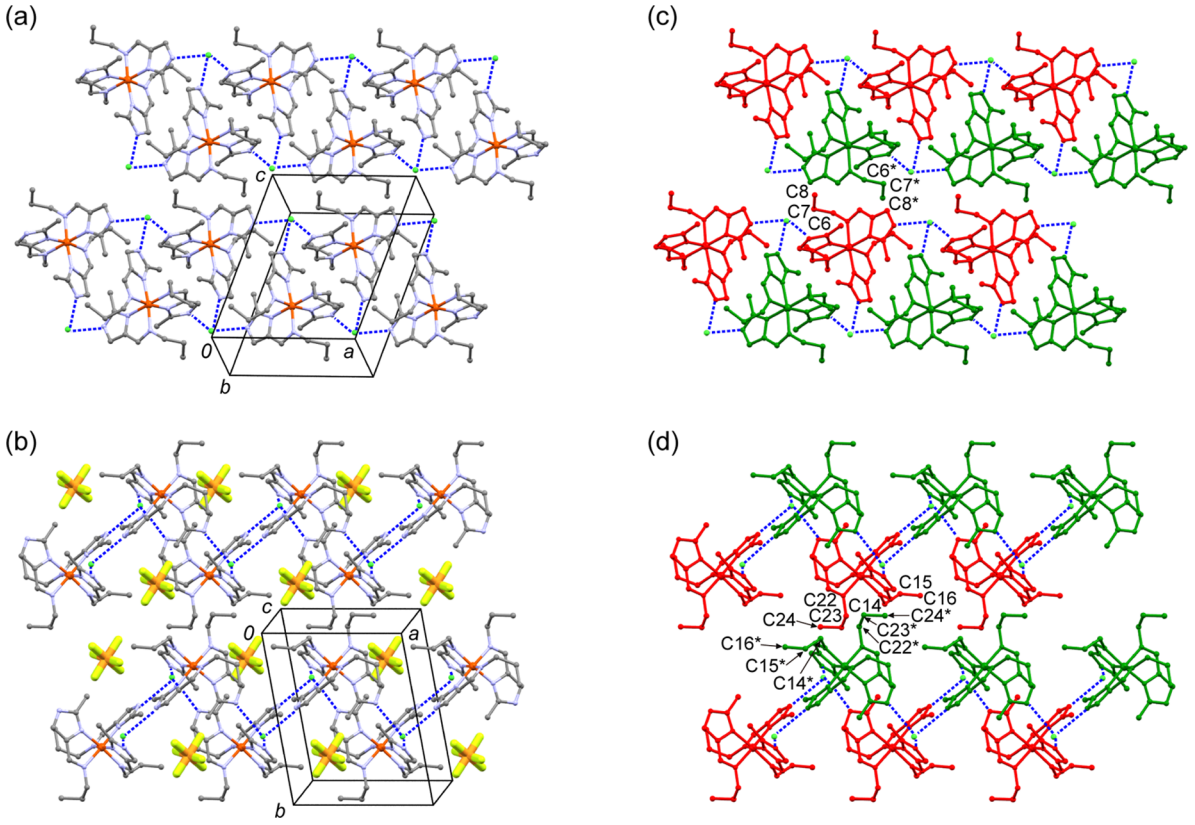

Figure 5. (a) Packing manner of the adjacent ladders of 1D ladder structure of *fac*-$[Fe^{II}(HL^{n\text{-}Pr})_3]Cl{\cdot}PF_6$ (**1**) projected on *ac*-plane. A 1D ladder structure runs along the *a*-axis. (b) Side view of stacking manner of the adjacent ladders and accommodation of PF_6^- anions. (c) Packing manner of the adjacent ladders. Two enantiomorphs of *fac*-Δ-$[Fe^{II}(HL^{n\text{-}Pr})_3]^{2+}$ (green) and *fac*-Λ-$[Fe^{II}(HL^{n\text{-}Pr})_3]^{2+}$ (red) are connected alternately by the intermolecular NH···Cl^- hydrogen-bonds to form a 1D ladder. (d) Stacking manner of two adjacent 1D ladders in a crystal, showing the array of the chirality of 1D ladders.

by green and red molecules, respectively. Within a ladder, Δ- and Λ-enantiomorphs connected by the Cl^-···NH hydrogen-bond are alternately arrayed. One side of the 1D ladder consists of the species with the same chirality, and the other side consists of the species with opposite chirality. Figure 5c shows the packing manner of the adjacent ladders extended on the *ac*-plane and the adjacent ladders of the opposite chiral species showing the array of the chiralities of 1D ladders. Figure 5d shows the stacking manner of the adjacent ladders along the *b*-axis, in which the upper side of the 1D ladder consists of the species with the same chirality and the lower side consists of the species with opposite chirality. The stacking of the ladders along the *b*-axis shows that the green and red layers are alternately arrayed. There are no noteworthy interladder interactions.

Crystal Structural Change of *fac*-$[Fe^{II}(HL^{n\text{-}Pr})_3]Cl{\cdot}PF_6$ (1) During Spin Transition Process. The X-ray diffraction data were collected so as to follow the SCO process of HS → $HS(T_1)$ → $HS(T_2)$ → low-spin LS → $LS(T_2)$ → $LS(T_1)$ → HS obtained by the magnetic susceptibility measurements. The crystal structures were determined at 160 (**a**), 143 (**b**), 120 (**c**), 110 (**d**), 95 (**e**) K in the cooling mode, and 110 (**f**), 120 (**g**), and 130 (**h**) K. In the cooling mode, the magnetic susceptibilities at the slowest scan speed of 0.1 K min^{-1} indicated HS at 160 K and HS at 143 K, HS (T_1 region) at 120 K, relaxation from HS to LS state (T_2 region) at 110 K, and LS at 95 K, respectively. In the warming mode from 95 K, the magnetic susceptibilities at 0.1 K min^{-1} indicated LS state at 110 K (T_2 relaxation region), LS at 120 K (T_1 relaxation region), and HS states at 130 K, respectively. The crystal was cooled from one to another temperature at a rate of 1 K min^{-1}, and the X-ray diffraction analysis started after the crystal was kept at the temperature for 3 h. In the warming mode, the crystal was warmed at a rate of 0.1 K min^{-1} and was kept at the temperature for 3 h, and then X-ray analysis was started.

The spin states at the temperatures are examined by the structural parameters. As given in Table 2, the unit cell volume decreases from 1628.4(2) $Å^3$ at 160 K (**a**) to 1555.0(4) $Å^3$ at 95 K (**e**) by 4.5% (1−1555.0/1628.4), whose value is in the range of the spin transition of the related Fe^{II} SCO complexes.[1,8,10] Compared with the cell dimensions at 160 K (**a**) and 95 K (**e**) in the cooling mode, the decreased dimensions in the *a*-axis (−0.079 Å) and *c*-axis (−0.121 Å) are larger than that in the *b*-axis (+0.003 Å). As seen in Figure 5a,b, the stepwise ladder runs along the *a*-axis, the ladder is extended to *ac*-plane, and adjacent ladders are stacked along the *b*-axis. The shortening of the Fe−N bond distances from the HS to LS spin transition propagates mainly to the *ac*-plane. These data indicate that the structural change during the spin transition occurs mainly within a ladder and interladder interaction must be very small. As shown in Table 1, the cell angles of β ($a \wedge c$) and γ ($a \wedge b$) become significantly smaller from the HS states ((**a**), (**b**), (**c**), and (**h**)) to LS states ((**e**), (**f**)), while α ($b \wedge c$) shows no noteworthy change. It is in accord with the ladder structure running along the *a*-axis is shrank as the spin transition from HS to LS. The cell parameters of (**d**) and (**g**) do not go along with the tendency, suggesting that something else exists at these states. The stepwise structure provides void-spaces for

DOI: 10.1021/acs.inorgchem.5b00701
Inorg. Chem. 2015, 54, 7291−7300

accommodation of PF_6^- anions, where PF_6^- anions suffer from disorder in the HS states. The void space becomes smaller, associated with the spin transition, and the PF_6^- anions have no disorder in the LS state.

The HS structures at 160 K (**a**), 143 K (**b**), and 120 K (**c**) in the cooling mode showed no significant differences in the coordination environment, the conformation of three propyl groups, and disorder of the PF_6^- anion. Figure 6A displays the

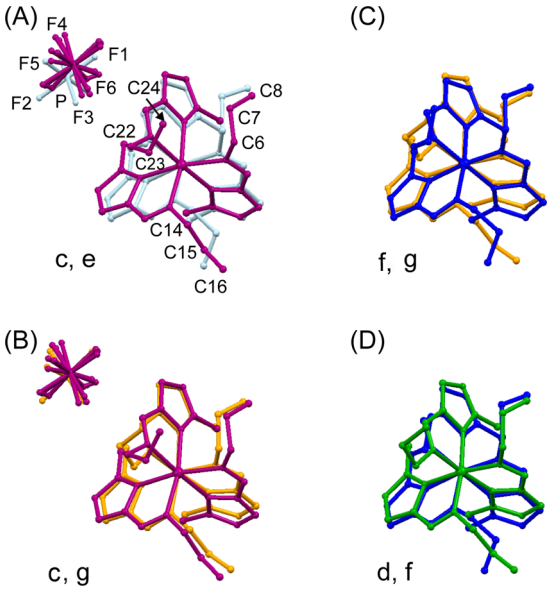

Figure 6. (A) Minimized overlay of cation and anion in HS state (purple) at 120 K (**c**) and LS state (light blue) at 95 K (**e**) in the cooling mode. (B) Minimized overlay of cation and anion in HS state (purple) at 120 K (**c**) of T_1 region in the cooling mode and LS2 state at 120 K (orange) (**g**) of T_2 regions in the warming mode. (C) Minimized overlay of cation in LS state (blue) at 110 K (**f**) and LS state (orange) at 120 K (**g**) in the warming mode. (D) Minimized overlay of cation in LS state (green) at 110 K (**d**) in the cooling mode and LS state (blue) at 110 K (**f**) in the warming mode.

minimized overlay of the complex-cation and anion in HS state at 120 K (**c**) and LS state at 95 K (**e**) in the cooling mode. The average Fe−N bond distance decreases from 2.193(3) Å at 120 K (**c**) to 1.982(6) Å (**e**) at 95 K by 0.21 Å, and the average N−Fe−N chelate angle changes from 77.3(1)° at 120 K (**c**) to 81.8(2)° (**e**) at 95 K by 4.5° to regular octahedron. The structural change is associated with the spin transition from the HS and LS state. In addition to the structural change of the FeN_6 coordination environment, the PF_6^- anion suffered from disorder in the HS state (**c**), but no disorder in the LS state (**e**); the conformation of one of three *n*-propyl groups (C6−C8) remains unchanged, but the remaining two *n*-propyl groups (C14−C16 and C22−C24) showed the significant conformational changes. A PF_6^- anion is accommodated in a cavity formed by the stepwise ladder structure, where the cavity is surrounded by two *n*-propyl groups (C14−C16 and C22−C24). The structure change in the FeN_6 coordination sphere propagates to the hydrogen-bonded ladder structure. Also, the order/disorder of the PF_6^- anion must be related to the conformational changes of two *n*-propyl groups.

Figure 6B displays the minimized overlay of the complex-cation at 120 K (T_1 region) in the cooling (**c**) and warming (**g**) modes. Complex **1** has a hysteresis loop so that the structural analyses for the top and bottom of the hysteresis loop at the same temperature are informative. The cell volumes at 120 K (T_1 region) in the cooling (**c**) and warming (**g**) modes are 1614.2(2) and 1563.3(5) $Å^3$, whose values indicate the HS and LS states, respectively. The coordination bond distances and angles are indicative of the spin state. The average Fe−N distance at 120 K decreases by 0.206 Å from 2.193(3) Å in the cooling mode to 1.987(6) Å in the warming mode. The N−Fe−N bond angles also indicate that the spin states are in the HS and LS states in the cooling and warming modes, respectively, as exemplified by a bite angle of N2−Fe−N3: 77.26(9)° in the cooling mode and 81.7(3)° in the warming mode. Further, the two *n*-propyl groups (C14−C16, C22−C24) showed the significant move in the conformations during the spin transition, and the PF_6^- anion showed no disorder at (**g**) while the disorder is at (**c**). On the basis of the examination of the bond distances and angles by the X-ray structural analyses, it is concluded that the spin states at 120 K (T_1 region) are HS and LS states in the cooling and warming modes, respectively. At 120 K in the T_1 temperature region, the magnetic susceptibility, Mössbauer, and single-crystal X-ray analyses measurements agreed well in the HS (**c**) in the cooling and in the LS state (**g**) in the warming mode.

Figure 6C displays the minimized overlay of the complex-cation at 110 K (**f**) of T_2 region and 120 K (**g**) of T_1 regions in the warming mode. The magnetic susceptibility data, Mössbauer data, and the X-ray data all demonstrated that complex **1** is in the LS state. Cell volumes (1563.1(7) at 110 K (**f**) of T_2 region and 1563.3(5) Å) at 120 K (**g**) of T_1 regions are almost similar to each other, but the cell parameter, especially γ (77.102(7)° for (**f**) and 83.818(4)° for (**g**)), shows a significant difference. The Fe−N bond angle and N−Fe−N angles are in the range of those for LS Fe^{II} complexes with similar nitrogen ligands, and there is no disorder at PF_6^- anion. While the complex **1** is in the LS state at T_1 and T_2 regions, there are remarkable structural differences at two *n*-propyl groups (C14−C16, C22−C24).

Figure 6D displays the minimized overlay of the complex-cation at 110 K (T_2 region) in the cooling (**d**) and warming (**f**) modes. The cell volumes at 110 K (T_2 region) are 1595(3) $Å^3$ (**d**) and 1563.1(7) $Å^3$ (**f**), respectively, where the standard deviations of the cell parameters and structural dimensions of (**d**) and (**f**) are both extremely large compared to those at other temperatures. The average Fe−N distance of 2.008(13) Å of (**d**) is a little longer than the LS distance and that of 1.990(10) Å of (**f**) is in the LS state. These results indicate that the structure of (**d**) at 110 K (T_2 region) in the cooling mode is changing during the X-ray data collection due to the relaxation from the HS to LS states. The temperature dependent magnetic susceptibility measurement at the slowest scan speed of 0.1 K min^{-1} takes several hours to sweep the T_2 region, whose procedure only detects a small sign of the relaxation from HS to LS at 110 K, as shown in Figure 7. It takes half a week for the Mössbauer data collection at 110 K (T_2 region), where only the LS state is detected due to the relaxation from HS to LS being completed. On the other hand, the X-ray data collection starts after the crystal was kept at 110 K for 6 h, and further it takes half a day to complete the X-ray data collection. With respect to the time measurement at the temperature, the X-ray data collection is an intermediate between the magnetic susceptibility at the slowest scan speed and the Mössbauer measurement. During the X-ray data collection the relaxation is occurring, and the X-ray analysis sees the result of the relaxation process from HS to LS. The structural parameters of

DOI: 10.1021/acs.inorgchem.5b00701
Inorg. Chem. 2015, 54, 7291−7300

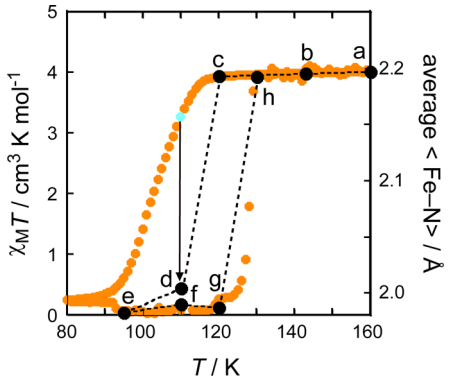

Figure 7. Average Fe−N bond distance (black ●) versus T of *fac*-$[Fe^{II}(HL^{n\text{-}Pr})_3]Cl{\cdot}PF_6$ (**1**) at 160 K (**a**), 143 K (**b**), 120 K (**c**), 110 K (**d**), and 95 K (**e**) in the cooling mode and at 110 K (**f**), 120 K (**g**), and 130 K (**h**) in the warming mode, together with the plots of $\chi_M T$ versus T (orange) measured at 0.1 K min^{-1}.

(**f**) at 110 K in the warming mode indicate that complex **1** is in LS state, but the standard deviations are extremely large. As seen in Figure 6C, the conformations of the propyl groups are different between the LS states of T_2 and T_1 phases and the structure changes at 110 K from T_2 to T_1 phase in the warming mode, as seen in Figure 7. The large standard deviations of (**f**) suggest that the structural phase transition from T_2 to T_1 phase begins at 110 K in the warming mode.

CONCLUDING REMARKS

In this study, solvent-free spin crossover Fe^{II} complex with the formula of *fac*-$[Fe^{II}(HL^{n\text{-}Pr})_3]Cl{\cdot}PF_6$ ($HL^{n\text{-}Pr}$ = 2-methylimidazol-4-yl-methylideneamino-*n*-propyl) was synthesized and studied. The magnetic susceptibility measurements at the scan speed of 0.5 K min^{-1} showed two successive spin transition processes consisting of the first spin transition T_1 around 120 K ($T_{1\uparrow}$ = 127.1 K, $T_{1\downarrow}$ = 115.8 K) and the second spin transition T_2 around 105 K ($T_{2\uparrow}$ = 115.8 K, $T_{2\downarrow}$ = 97.2 K). The magnetic susceptibility measurements at the scan speed of 0.5 K min^{-1} detected two successive spin transition processes, while the Mössbauer spectra detected only T_1. The magnetic susceptibility measurements at the scan rate of 2.0, 1.0, 0.5, 0.25, and 0.1 K min^{-1} showed two scan speed dependent spin transitions, in which as the scan speed decreases, the spin transition of T_2 is disappearing due to the relaxation from HS to LS of T_2, and on the contrary, the spin transition of T_1 from LS to HS is pronounced. The exposure time before the measurement and the measuring time at the temperature are different among the physical measurements. It demonstrates that the second spin transition T_2 exhibits a relaxation process which is observable for the measuring time of the magnetic susceptibility but not for those of the Mössbauer spectra measurements, and the conventional single-crystal X-ray diffraction analysis has an intermediate measuring time. The crystal structures were determined so as to follow the spin transition process. Three imidazole groups of *fac*-$[Fe^{II}(HL^{n\text{-}Pr})_3]^{2+}$ are hydrogen-bonded to three Cl^- ions, and the resulting 3:3 NH(imidazole)···Cl^- hydrogen-bonds produce a stepwise ladder structure. The structures at 120 K in the T_1 region in the cooling and heating modes showed typical HS and LS structural characters, respectively. The structures at 110 K in the T_2 region in the heating modes showed typical LS characters, but that in the cooling mode showed an intermediate character between the HS and LS states due to the relaxation. The structural information for two successive spin transitions with thermal hysteresis and relaxation process is well-obtained, probably due to the ladder structure constructed by the hydrogen-bonds. The present compound and the analogous Fe^{II} complexes[16] are likely to exhibit the relaxation process as well as hysteresis. This property should be related to the assembly structure constructed by NH···Cl^- hydrogen-bonds, subtle structural changes in the counteranion and alkyl groups, and the packing manner. It is expected that the analogous Fe^{II} complexes can give interesting SCO properties such as the relaxation process and large thermal hysteresis. Further studies can give insight into understanding the detailed SCO mechanism based on the experimental data.

ASSOCIATED CONTENT

Supporting Information

Additional figure demonstrating hysteresis. X-ray crystallographic files (CIFs) for *fac*-$[Fe^{II}(HL^{n\text{-}Pr})_3]Cl{\cdot}PF_6$ (**1**) at 160, 143, 120, 110, and 95 K in the cooling mode, and 110, 120, and 130 K in the warming mode as CCDC numbers 1054920−1054927. The Supporting Information is available free of charge on the ACS Publications website at DOI: 10.1021/acs.inorgchem.5b00701. Crystallographic files also available upon application to the Cambridge Crystallographic data Centre, 12 Union Road, Cambridge CB2 1EZ, U.K. [fax (+44)1223-336-033; e-mail deposit@ccdc.cam.ac.uk].

AUTHOR INFORMATION

Corresponding Authors

*E-mail: naohide@aster.sci.kumamoto-u.ac.jp.
*E-mail: sunatuki@okayama-u.ac.jp.

Notes

The authors declare no competing financial interest.

ACKNOWLEDGMENTS

We would like to thank Tomohiro Ohishi and Satoh Tetsuya at Engineering Research Equipment Center, Kumamoto University, for their X-ray powder pattern measurements. T.F. and K.N. were supported by the Research Fellowship of the Japan Society for the Promotion of Science, KAKENHI 00248556 and 00248498. Y.S. acknowledges a support from Grant-in-Aid for Scientific Research from the Ministry of Education, Science, Sports and Culture of Japan (Basic Research (C) 15K05455).

REFERENCES

(1) (a) *Spin Crossover in Transition Metal Compounds I–III*; Gütlich, P., Goodwin, H. A., Eds.; Springer: New York, 2004. (b) Decurtins, S.; Gütlich, P.; Köhler, C. P.; Spiering, H.; Hauser, A. *Chem. Phys. Lett.* **1984**, *105*, 1−4. (c) Gütlich, P.; Garcia, Y.; Woike, T. *Coord. Chem. Rev.* **2001**, *219−221*, 839−879. (d) Real, J. A.; Gaspar, A. B.; Munoz, M. C. *Dalton Trans.* **2005**, 2062−2079. (e) Gütlich, P.; Gaspar, A. B.; Garcia, Y. *Beilstein J. Org. Chem.* **2013**, *9*, 342−391.

(2) (a) Kahn, O.; Martinez, J. C. *Science* **1998**, *279*, 44−48. (b) Dirtu, M. M.; Neuhausen, C.; Naik, A. D.; Rotaru, A.; Spinu, L.; Garcia, Y. *Inorg. Chem.* **2010**, *49*, 5723−5736. (c) Garcia, Y.; Moscovici, J.; Michalowicz, A.; Ksenofontov, V.; Levchenko, G.; Bravic, G.; Chasseau, D.; Gütlich, P. *Chem. - Eur. J.* **2002**, *8*, 4992−5000. (d) Lochenie, C.; Bauer, W.; Railliet, A. P.; Schlamp, S.; Garcia, Y.; Weber, B. *Inorg. Chem.* **2014**, *53*, 11563−11572.

(3) (a) Weber, B.; Bauer, W.; Obel, J. *Angew. Chem., Int. Ed.* **2008**, *47*, 10098−10101. (b) Weber, B. *Coord. Chem. Rev.* **2009**, *253*, 2432−2449.

(4) (a) Ross, T. M.; Neville, S. M.; Innes, D. S.; Turner, D. R.; Moubaraki, B.; Murray, K. S. *Dalton Trans.* **2010**, *39*, 149−159.

DOI: 10.1021/acs.inorgchem.5b00701
Inorg. Chem. 2015, 54, 7291−7300

(b) Wu, D.-Y.; Sato, O.; Einaga, Y.; Duan, C.-Y. *Angew. Chem., Int. Ed.* **2009**, *48*, 1475−1478. (c) Ruben, M.; Breuning, E.; Lehn, J.-M.; Kseno-fontov, V.; Renz, F.; Gütlich, P.; Vaughan, G. B. M. *Chem. - Eur. J.* **2003**, *9*, 4422−4429. (d) Nowak, R.; Bauer, W.; Ossiander, T.; Weber, B. *Eur. J. Inorg. Chem.* **2013**, *2013*, 975−983. (e) Imatomi, S.; Sato, T.; Hamamatsu, T.; Kitashima, R.; Matsumoto, N. *Bull. Chem. Soc. Jpn.* **2007**, *80*, 2375−2377. (f) Fujinami, T.; Nishi, K.; Kitashima, R.; Murakami, K.; Matsumoto, N.; Iijima, S.; Toriumi, K. *Inorg. Chim. Acta* **2011**, *376*, 136−143.

(5) (a) Buchen, T.; Gütlich, P.; Sugiyarto, K. H.; Goodwin, H. A. *Chem. - Eur. J.* **1996**, *2*, 1134−1138. (b) Sugiyarto, K. H.; Scudder, M. L.; Craig, D. C.; Goodwin, H. A. *Aust. J. Chem.* **2000**, *53*, 755−765. (c) Sato, T.; Nishi, K.; Iijima, S.; Kojima, M.; Matsumoto, N. *Inorg. Chem.* **2009**, *48*, 7211−7229. (d) Yamada, M.; Hagiwara, H.; Torigoe, H.; Matsumoto, N.; Kojima, M.; Dahan, F.; Tuchagues, J.-P.; Re, N.; Iijima, S. *Chem. - Eur. J.* **2006**, *12*, 4536−4549. (e) Furushou, D.; Hashibe, T.; Fujinami, T.; Nishi, K.; Hagiwara, H.; Matsumoto, N.; Sunatsuki, Y.; Kojima, M.; Iijima, S. *Polyhedron* **2012**, *44*, 194−203.

(6) (a) Létard, J.-F.; Guionneau, P.; Codjovi, E.; Lavastre, O.; Bravic, G.; Chasseau, D.; Kahn, O. *J. Am. Chem. Soc.* **1997**, *119*, 10861−10862. (b) Zhong, Z. J.; Tao, J.-Q.; Yu, Z.; Dun, C.-Y.; Lui, Y.-J.; You, X.-Z. *J. Chem. Soc., Dalton Trans.* **1998**, 327−328. (c) Hagiwara, H.; Hashimoto, S.; Matsumoto, N.; Iijima, S. *Inorg. Chem.* **2007**, *46*, 3136−3143. (d) Breuning, E.; Ruben, M.; Lehn, J.-M.; Renz, F.; Garcia, Y.; Ksenofontov, V.; Gütlich, P.; Wegelius, E.; Rissanen, K. *Angew. Chem., Int. Ed.* **2000**, *39*, 2504−2507.

(7) (a) Kitazawa, T.; Gomi, Y.; Takahashi, M.; Takeda, M.; Enomoto, M.; Miyazaki, A.; Enoki, T. *J. Mater. Chem.* **1996**, *6*, 119−121. (b) Rodriguez-Velamazan, J. A.; Castro, M.; Palacios, E.; Burriel, R.; Kitazawa, T.; Kawasaki, T. *J. Phys. Chem. B* **2007**, *111*, 1256−1261. (c) Rodriguez-Velmazan, J. A.; Carbonera, C.; Castro, M.; Palacios, E.; Kitazawa, T.; Letard, J.-F.; Burriel, R. *Chem. - Eur. J.* **2010**, *29*, 8785−8796. (d) Galet, A.; Munoz, M. C.; Gaspar, A. B.; Real, J. A. *Inorg. Chem.* **2005**, *44*, 8749−8755. (e) Ohba, M.; Yoneda, K.; Agustí, G.; Muñoz, M. C.; Gaspar, A. B.; Real, J. A.; Yamasaki, M.; Ando, H.; Nakao, Y.; Sakaki, S.; Kitagawa, S. *Angew. Chem., Int. Ed.* **2009**, *48*, 4767−4771.

(8) (a) Cook, L. J. K.; Shepherd, H. J.; Comyn, T. P.; Balde, C.; Cespedes, C.; Chastanet, G.; Halcrow, M. A. *Chem. - Eur. J.* **2015**, *21*, 4805−4816. (b) Matouzenko, G. S.; Bousseksou, A.; Borshch, S. A.; Perrin, M.; Zein, S.; Salmon, L.; Molnar, G.; Lecocq, S. *Inorg. Chem.* **2004**, *43*, 227−236. (c) Money, V. A.; Elhaïk, J.; Evans, I. R.; Halcrow, M. A.; Howard, J. A. K. *Dalton Trans.* **2004**, 65−69.

(9) (a) Ikuta, Y.; Ooidemizu, M.; Yamahata, Y.; Yamada, M.; Osa, S.; Matsumoto, N.; Iijima, S.; Sunatsuki, Y.; Kojima, M.; Dahan, F.; Tuchagues, J.-P. *Inorg. Chem.* **2003**, *42*, 7001−7017. (b) Sunatsuki, Y.; Ohta, H.; Kojima, M.; Ikuta, Y.; Goto, Y.; Matsumoto, N.; Iijima, S.; Akashi, H.; Kaizaki, S.; Dahan, F.; Tuchagues, J.-P. *Inorg. Chem.* **2004**, *43*, 4154−4171. (c) Yamada, M.; Ooidemizu, M.; Ikuta, Y.; Osa, S.; Matsumoto, N.; Iijima, S.; Kojima, M.; Dahan, F.; Tuchagues, J.-P. *Inorg. Chem.* **2003**, *42*, 8406−8416. (d) Bréfuel, N.; Imatomi, S.; Torigoe, H.; Hagiwara, H.; Shova, S.; Meunier, J.-F.; Bonhommeau, S.; Tuchagues, J.-P.; Matsumoto, N. *Inorg. Chem.* **2006**, *45*, 8126−8135. (e) Nishi, K.; Arata, S.; Matsumoto, N.; Iijima, S.; Sunatsuki, Y.; Ishida, H.; Kojima, M. *Inorg. Chem.* **2010**, *49*, 1517−1523. (f) Hashibe, T.; Fujinami, T.; Furusho, D.; Matsumoto, N.; Sunatsuki, S. *Inorg. Chim. Acta* **2011**, *375*, 338−342.

(10) (a) Brewer, C. T.; Brewer, G.; Butcher, R. J.; Carpenter, E. E.; Schmiedekamp, A. M.; Viragh, C. *Dalton Trans.* **2007**, 295−298. (b) Brewer, C. T.; Brewer, G.; Luckett, C.; Marbury, G. S.; Viragh, C.; Beatty, A. M.; Scheidt, W. R. *Inorg. Chem.* **2004**, *43*, 2402−2415. (c) Brewer, C. T.; Brewer, G.; Butcher, R. J.; Carpenter, E. E.; Cuenca, L.; Schmiedekamp, A. M.; Viragh, C. *Dalton Trans.* **2005**, 3617−3619.

(11) (a) Fujinami, T.; Nishi, K.; Matsumoto, N.; Iijima, S.; Halcrow, M. A.; Sunatsuki, Y.; Kojima, M. *Dalton Trans.* **2011**, *40*, 12301−12309. (b) Nishi, K.; Matsumoto, N.; Iijima, S.; Halcrow, M. A.; Sunatsuki, Y.; Kojima, M. *Inorg. Chem.* **2011**, *50*, 11303−11305.

(12) (a) Kulmaczewski, R.; Olguín, J.; Kitchen, J. A.; Feltham, H. L. C.; Jameson, G. N. L.; Tallon, J. F.; Brooker, S. *J. Am. Chem. Soc.* **2014**, *136*, 878−881. (b) Seredyuk, M.; Munoz, M. C.; Castro, M.; Romero-Morcillo, T.; Gaspar, A. B.; Real, J. A. *Chem. - Eur. J.* **2013**, *19*, 6591−6596. (c) Yamasaki, M.; Ishida, T. *J. Mater. Chem. C* **2015**, DOI: 10.1039/C5TC00926J.

(13) Kahn, O.; *Molecular Magnetism*; VCH: Weinheim, Germany, 1993.

(14) MossWinn−Mössbauer spectrum analysis and database software. http://www.Mosswinn.com/.

(15) *CrystalStructure 4.0: Crystal Structure Analysis Package*; Rigaku Corporation: Tokyo, 2000−2010.

(16) Nishi, K.; Kondo, H.; Fujinami, T.; Matsumoto, N.; Iijima, S.; Halcrow, M. A.; Sunatsuki, Y.; Kojima, M. *Eur. J. Inorg. Chem.* **2013**, *2013*, 927−933.

DOI: 10.1021/acs.inorgchem.5b00701
Inorg. Chem. 2015, 54, 7291−7300